

Geometry-Aware Reference Synthesis for Multi-View Image Super-Resolution

Ri Cheng

School of Computer Science,
Shanghai Key Laboratory of
Intelligent Information Processing,
Shanghai Collaborative Innovation
Center of Intelligent Visual
Computing, Fudan University
Shanghai, China
rcheng20@fudan.edu.cn

Yuqi Sun

School of Computer Science,
Shanghai Key Laboratory of
Intelligent Information Processing,
Shanghai Collaborative Innovation
Center of Intelligent Visual
Computing, Fudan University
Shanghai, China
yqsun20@fudan.edu.cn

Bo Yan*

School of Computer Science,
Shanghai Key Laboratory of
Intelligent Information Processing,
Shanghai Collaborative Innovation
Center of Intelligent Visual
Computing, Fudan University
Shanghai, China
byan@fudan.edu.cn

Weimin Tan

School of Computer Science,
Shanghai Key Laboratory of
Intelligent Information Processing,
Shanghai Collaborative Innovation
Center of Intelligent Visual
Computing, Fudan University
Shanghai, China
wmtan@fudan.edu.cn

Chenxi Ma

School of Computer Science,
Shanghai Key Laboratory of
Intelligent Information Processing,
Shanghai Collaborative Innovation
Center of Intelligent Visual
Computing, Fudan University
Shanghai, China
17210240039@fudan.edu.cn

ABSTRACT

Recent multi-view multimedia applications struggle between high-resolution (HR) visual experience and storage or bandwidth constraints. Therefore, this paper proposes a Multi-View Image Super-Resolution (MVISR) task. It aims to increase the resolution of multi-view images captured from the same scene. One solution is to apply image or video super-resolution (SR) methods to reconstruct HR results from the low-resolution (LR) input view. However, these methods cannot handle large-angle transformations between views and leverage information in all multi-view images. To address these problems, we propose the MVSNet, which uses geometry information to extract sharp details from all LR multi-view to support the SR of the LR input view. Specifically, the proposed Geometry-Aware Reference Synthesis module in MVSNet uses geometry information and all multi-view LR images to synthesize pixel-aligned HR reference images. Then, the proposed Dynamic High-Frequency Search network fully exploits the high-frequency textural details in reference images for SR. Extensive experiments on several benchmarks show that our method significantly improves over the state-of-the-art approaches.

*Corresponding Author. This work is supported by NSFC (Grant No.: U2001209, 61902076) and Natural Science Foundation of Shanghai (21ZR1406600).

Permission to make digital or hard copies of all or part of this work for personal or classroom use is granted without fee provided that copies are not made or distributed for profit or commercial advantage and that copies bear this notice and the full citation on the first page. Copyrights for components of this work owned by others than ACM must be honored. Abstracting with credit is permitted. To copy otherwise, or republish, to post on servers or to redistribute to lists, requires prior specific permission and/or a fee. Request permissions from permissions@acm.org.

MM '22, October 10–14, 2022, Lisbon, Portugal.

© 2022 Association for Computing Machinery.

ACM ISBN 978-1-4503-9203-7/22/10...\$15.00

<https://doi.org/10.1145/3503161.3547947>

CCS CONCEPTS

• Computing methodologies → Computer vision; Reconstruction.

KEYWORDS

Super-resolution, Multi-view images

ACM Reference Format:

Ri Cheng, Yuqi Sun, Bo Yan, Weimin Tan, and Chenxi Ma. 2022. Geometry-Aware Reference Synthesis for Multi-View Image Super-Resolution. In *Proceedings of the 30th ACM International Conference on Multimedia (MM '22), October 10–14, 2022, Lisbon, Portugal*. ACM, New York, NY, USA, 17 pages. <https://doi.org/10.1145/3503161.3547947>

1 INTRODUCTION

Multi-view Multimedia (MVMM) uses numerous cameras to capture multi-view images of the same scene from various angles. It is widely used in auto-driving, street-view navigation, free-viewpoint video[17, 36], and virtual reality[1, 3]. Recent MVMM applications call for high-resolution (HR) images to give a pleasing visual experience and assist downstream tasks such as detection and tracking. Nevertheless, HR multi-view images face substantial storage costs or bandwidth constraints. To address this problem, we propose the Multi-View Image Super-Resolution (MVISR) task, which increases the resolution of multi-view images by using all low-resolution (LR) multi-view images in the same scene.

A naive approach to MVISR is to perform single image SR (SISR) [6, 21] on each view. They take a single view as input and cannot utilize the relationship across all LR views. Other alternatives include video SR (VSR) methods [4, 18]. They regard multi-views as video

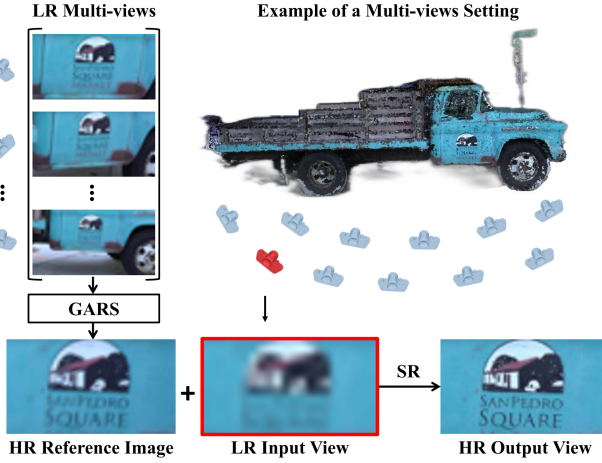


Figure 1: Multi-view image super-resolution. We propose GARS module for extracting the HR details from all LR Multi-View. Then, our GARS module synthesizes high-frequency textural details into HR Reference Image that is aligned with the bicubic of LR Input View. The word SQUARE is more textured in HR Reference Image than in the LR Input View.

frames with little object motion, and so cannot deal with the large-angle transformations between input views. Some reference-based SR (Ref-SR) methods [23, 45, 52] can overcome angle constraints and extend the range of reference views. However, Ref-SR is ineffective due to the difficulties involved with reference image selection in all LR multi-views and reference alignment when the scale and rotation differences between the Ref and LR input are large. In the end, none of the approaches discussed previously can explicitly leverage all LR multi-views and their associated geometry information.

Therefore, in this paper, we propose MVSNet, which utilizes the geometry information to exploit high-frequency (HF) reference information from all LR views for each view SR. A camera that is closer to the objects can capture sharper images than a distant one. It inspires us that a close-up view contains more textural details that can provide sufficient reference for the distant view. To realize this idea, we design Geometry-Aware Reference Synthesis (GARS) module in MVSNet. As illustrated in Figure 1, the word SQUARE is blurred in the LR input view but sharp in other LR views. Our GARS module takes LR multi-views as input to generate reference images with rich textural details and well-aligned with the LR input view. To be specific, we use structure-from-motion [31] and multi-view stereo [32, 46] to extract scene geometry information such as the camera pose and depth map. After that, GARS conducts 3D image warping to align all LR multi-views into the target view. Then, we introduce a depth-guided patch-selection strategy to select close views on the patch level and fuse them into HR multi-view reference images (MVRs).

On the other hand, MVRs synthesized from all LR views in GARS have artifacts and some pixels that are not properly aligned with the LR input view due to inaccuracies in the geometry information. Nearby views have a small difference in viewing angle and hence

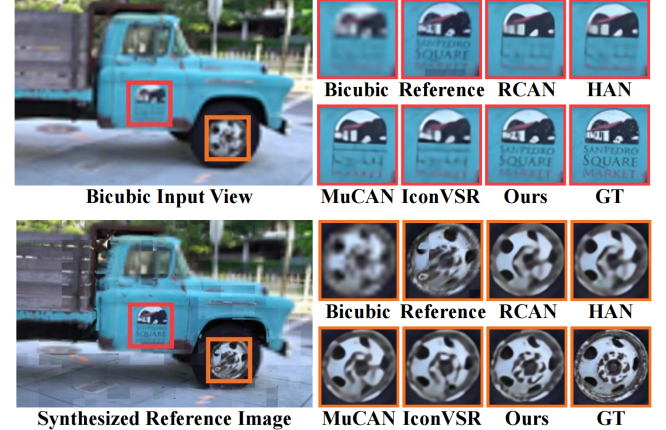


Figure 2: Example of multi-view image super-resolution results. Our proposed model outperforms SISR (RCAN [51]) and HAN [27]) and VSR (MuCAN [18] and IconVSR [4]) methods in visual quality. For instance, by utilizing the synthesized reference image, our model is able to recover finer details of the word SQUARE in the first example and the center area of the tire in the second example.

suffer less from geometric inaccuracies. As a result, we also synthesize near-view reference images (NVRs) with fewer artifacts but fewer HF textural details using nearby views. Then, in order to properly leverage MVRs and NVRs, we design the Raw Selection Module (RSM) and Adaptation Selection Module (ASM) in our Dynamic High-Frequency Search (DHFS) network to exploit the HF textural details by reducing the feature difference dynamically. Finally, we perform experiments to demonstrate the proposed MVSNet SR capability, and some comparative experiments are shown in Figure 2. Additionally, our work contributes to the Ref-SR methodology by proposing a way for performing SR using multi-view LR images rather than HR images [52] as reference.

This paper mainly has the following contributions:

- For the first time, this paper proposes the MVSNet, a learning-based network that makes explicit use of geometric information to address the MVSR problem. In addition, this work enriches the Reference-Based SR research.
- The Geometry-Aware Reference Synthesis module synthesizes the HR reference image from all LR multi-view images using geometry information. The reference supports SR by containing rich high-frequency textural details and aligning with the input view.
- The Dynamic High-Frequency Search network is proposed for reconstructing the high-resolution view by dynamically reducing the feature difference to exploit high-frequency textural details from synthesized reference images.

2 RELATED WORK

2.1 Single Image Super-Resolution

Single Image Super-Resolution (SISR) [6, 16, 21, 25, 41, 51] aims to learn the mapping function between LR and HR images. However,

SISR is unable to recover HF details due to the destruction of HR textural clues in the downsampling LR image.

2.2 Reference-Based Super-Resolution

Reference-based super-resolution (Ref-SR) approaches transfer the HR details of the reference image to the LR input image. Several works [34, 53] leverage deformable convolution [5, 54] or estimated flow to align and extract reference features. However, it will seriously affect the performance of these algorithms when finding long-distance correspondence. The patch-based Ref-SR approaches [13, 23, 44, 45, 52] perform patch matching in the feature space by calculating the cosine similarity between the LR patch and Ref patch. [23, 45] formulate patch matching based on the transformer [39]. However, the difference in scale and rotation between the HR Ref and LR inputs can cause matching errors [13], which is serious in multi-view settings. In addition, for the super-resolution of multi-view LR images, there is no available view reference selection method. The SIFT-based [22] selection method used in constructing the CUFED5 [52] dataset is only applicable to selecting HR references whose content is similar to the LR input view.

2.3 Multi-View Super-Resolution

Several traditional approaches [7, 38] and learning-based approaches [20, 28] study the multi-view texture SR problem. However, they only super-resolve the texture of the object instead of the entire image. Stereo image SR [40, 48] utilizes additional information provided from a second viewpoint, but it uses a much smaller number of viewpoint than MVISR. Light field image SR [2, 42, 43, 50] has also been extensively studied in recent years, but the view span are limited compared to the unstructured multi-views. Our MVSRnet differs from multi-view video SR [19, 24] in that they utilize HR reference frames, whereas MVSRnet exclusively uses LR frames. However, obtaining HR images is difficult due to substantial storage costs and bandwidth constraints in reality. Sun *et al.* [37] addresses the space-angle SR problem, but only two adjacent views are used to synthesize virtual view and SR. In general, it is difficult to apply the methods discussed above to the MVISR task directly.

3 PROPOSED METHOD

This section describes the proposed network called MVSRnet, and the overview of the MVSRnet is shown in Figure 3(a). We begin with a data preprocessing step that estimates depth maps $\{D_i^{lr}\}_{i=1}^S$ and poses $\{P_i^{lr}\}_{i=1}^S$ of all S LR multi-views in Section 3.1. Then, in Section 3.2, we introduce Geometry-Aware Reference Synthesis (GARS) that uses geometry priors $(\{D_i^{lr}\}_{i=1}^S, \{P_i^{lr}\}_{i=1}^S)$ to synthesize V HR multi-view reference (MVR) $\{R_i^M\}_{i=1}^V$ and HR near-view reference (NVR) $\{R_i^N\}_{i=1}^V$. MVR stores more high-frequency (HF) textural details than NVR since MVR is synthesised from all S LR multi-view images $\{I_i^{lr}\}_{i=1}^S$, not from L nearby views like NVR. However, there are fewer artifacts caused by erroneous warping in the NVR. Therefore, in Section 3.3, we design Dynamic High-Frequency Search (DHFS) network that dynamically selects and extracts the correct HF details in MVRs and NVRs to super-resolve the LR input view I_T^{lr} and get HR output view I_T^{hr} . At last, loss functions are shown in Section 3.4.

3.1 Preprocessing

To obtain the geometry information of the multi-view scene, we utilize COLMAP [31] to compute camera poses by inputting all S LR multi-views. This is known as structure-from-motion (SfM), and we can get the camera pose $\{P_i^{lr}\}_{i=1}^S$ of each viewpoint. The pose is represented by the extrinsic parameters (rotation matrices and translation vectors) and intrinsic parameters. We use the depth map of the LR input view to align all LR multi-views to the LR input view. Therefore, we conduct the multi-view stereo (MVS) in COLMAP to obtain the depth map for each LR view $\{D_i^{lr}\}_{i=1}^S$ by inputting all LR multi-views and the SfM output.

3.2 Geometry-Aware Reference Synthesis

The GARS module synthesizes references (Refs) from all multi-view images, and we display the synthesis process of a Ref in Figure 3(b). The reference image is aligned with the input view and contains high-frequency details.

Alignment Using Scene Geometry. When the reference image has a large deformation in comparison to the input image, the alignment capabilities of recent Ref-SR approaches are reduced. For instance, Figure 3 illustrates a great differences in scale and rotation of the truck between the LR input view I_T^{lr} and view I_S^{lr} . Therefore, we use the multi-view scene geometry to explicitly align all multi-view source images $\{I_i^{lr}\}_{i=1}^S$ with the input view I_T^{lr} . Specifically, we up-sample the depth map to the target output resolution (SR factor is $\times 4$ in our experiment setting) based on the bicubic mode and modify the camera intrinsic matrices according to the up-sampling factor. Then we apply the 3D warping operation [26] to obtain warped views $\{I_{i \rightarrow T}^{hr}\}_{i=1}^S$ as follows:

$$I_{i \rightarrow T}^{hr} = W \left(D_i^{hr}, D_T^{hr}, P_i^{hr}, P_T^{hr}, I_i^{lr} \right), \quad (1)$$

where i and T refer to i -th multi-view images and input view. D^{hr} and P^{hr} denote the depth maps and the camera pose at the same resolution as the target output solution. Specifically, the pixel coordinate correspondence between the multi-view images and the input view in the 3D warping operation is as the following formula:

$$D_i(p_i) * p_i = K_i(R_r K_T^{-1} D_T(p_T) * p_T + t_r), \quad (2)$$

where p denotes pixel homogeneous coordinates. Camera intrinsic matrices K , rotation matrices R and translation matrices t are provided by camera posed P as presented in Eq.(1). $R_r = R_i R_T^T$, $t_r = t_i - R_r t_T$ are relative rotation and translation matrices.

It is noted that we can directly apply 3D warping operation on LR depth maps without up-sampling and obtain LR aligned views $\{I_{i \rightarrow T}^{lr}\}_{i=1}^S$. However, the general sampling modes in warping operation, such as nearest and bilinear, blurs and deconstructs high-frequency details using the weighted average method when dealing with overlapping pixels. One possible solution is to use a pre-trained network as a feature extractor to conduct 3D warping operations in the LR feature space. However, this leads to both spatially and temporally inefficient as hundreds of views need to be extracted features in each training iteration.

HF Details Extraction Using Depth-Guided Patch-Selection Strategy. We should extract useful HF details from warped views $\{I_{i \rightarrow T}^{hr}\}_{i=1}^S$ that contain redundant details as the warped view contains the LR details area as well. We assume that the view taken at

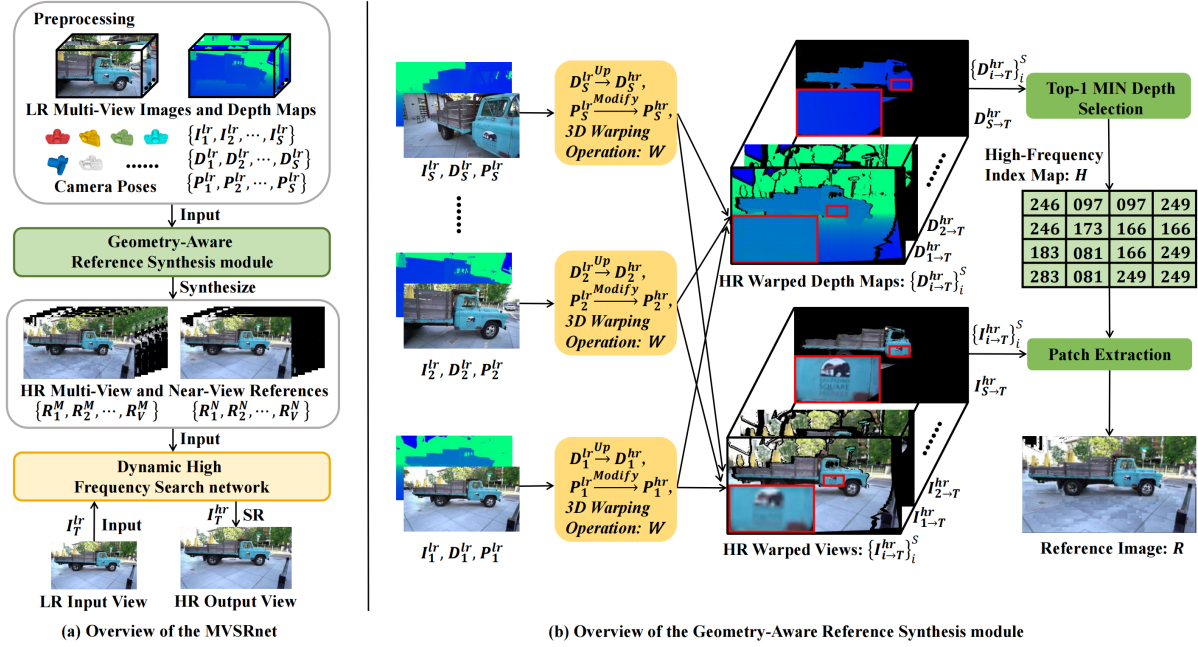


Figure 3: (a) The overview pipeline of the proposed MVSNet. (b) The depth value of truck door area in the warped depth map $D_{S \rightarrow T}^{hr}$ is smaller (darker blue) than $D_{1 \rightarrow T}^{hr}$, so the warped view $I_{S \rightarrow T}^{hr}$ contains more truck door HR details than $I_{1 \rightarrow T}^{hr}$, corresponding to more truck door high-frequency details in view $I_{S \rightarrow T}^{hr}$ than $I_{1 \rightarrow T}^{hr}$.

close range has more high-frequency textural details than the distant view. Therefore, we apply the 3D warping operation on source depth maps $W(D_i^{hr}, D_T^{hr}, P_i^{hr}, P_T^{hr}, D_i^{lr})$ to obtain HR warped depth maps $\{D_{i \rightarrow T}^{hr}\}_{i=1}^S$. Warped depth maps present distance geometry information, i.e., the distance between the object and the camera. The smaller the depth value, the closer the object in source view I_i^{lr} is to the camera. As a result, we can leverage the HR warped depth maps to locate the HR details area in the warped views $\{I_{i \rightarrow T}^{hr}\}_{i=1}^S$. For example, Figure 3(b) shows that the truck door has smaller depth values (darker blue) in the warped depth map $D_{S \rightarrow T}^{hr}$ than $D_{1 \rightarrow T}^{hr}$. Hence, the HR warped view $I_{S \rightarrow T}^{hr}$ contains more truck door HR details than $I_{1 \rightarrow T}^{hr}$, corresponding to more truck door high-frequency details in view $I_{S \rightarrow T}^{hr}$ than $I_{1 \rightarrow T}^{hr}$.

We unfold each warped depth map into patches $p_{i,j}$, $(i \in [1, S], j \in [1, (hr_h \times hr_w) / (ps^2)])$, hr_h , hr_w , and ps denote the target HR height, target HR width, and patch size. j denotes the j -th patch index. We also unfold each warped view, and denote it as $I_{i \rightarrow T,j}^{hr}$. Then, we assign the depth value in each patch to its patch mean $p_{i,j}^{mean} = mean(p_{i,j})$. This alleviates the error of the depth value averaged in the edge area due to the up-sampling and warping operation. Then, we obtain the high-frequency index map H from the index with the smallest depth value in $p_{i,j}^{mean}$ as follows:

$$H_j = \arg \min_i p_{i,j}^{mean}. \quad (3)$$

H_j refers to the high-frequency patch index of warped views, and we extract the high-frequency patch as the following formula:

$$R_j = I_{i \rightarrow T,j}^{hr}, \quad i = H_j. \quad (4)$$

Now we can obtain the multi-view reference image R by folding the multi-view reference patches R_j .

Multiple References Synthesis. It is impossible to integrate all of the high-frequency details into a reference image. As a result, we synthesize V multi-view reference images (MVRs) denoted as $\{R_i^M\}_{i=1}^V$ using those the top V high-frequency index maps. However, the depth errors generated by MVS estimation and 3D warping causes inaccurate warped depth values, leading to incorrect MVR selection and alignment. In addition, the large angle difference between views magnifies alignment errors, resulting artifacts in MVR. Therefore, we synthesize V near-view reference images (NVRs) $\{R_i^N\}_{i=1}^V$ from L nearby views that have a small viewing angle gap and similar lighting conditions as the LR input view. NVRs suffer less from geometric inaccuracies, and the selection criteria for nearby views are based on their order in the dataset. NVR includes less high-frequency details than MVR, but it also contains fewer alignment errors, and artifacts. As a result, both MVRs and NVRs can be used to cross-reference to correct selection errors and accurately supply HF details to the SR model.

3.3 Dynamic High-Frequency Search

MVR has both more HF textural details and more artifacts than NVR, and that NVR is the inverse. Therefore, we propose the DHFS network to maximize the use of references (MVR and NVR). As shown in Figure 4(a), we first concatenate the MVRs and NVRs to the bicubic input view at the channel level, and use a learnable feature extractor to extract their multi-scale ($\times 1$, $\times 2$, and $\times 4$) textural

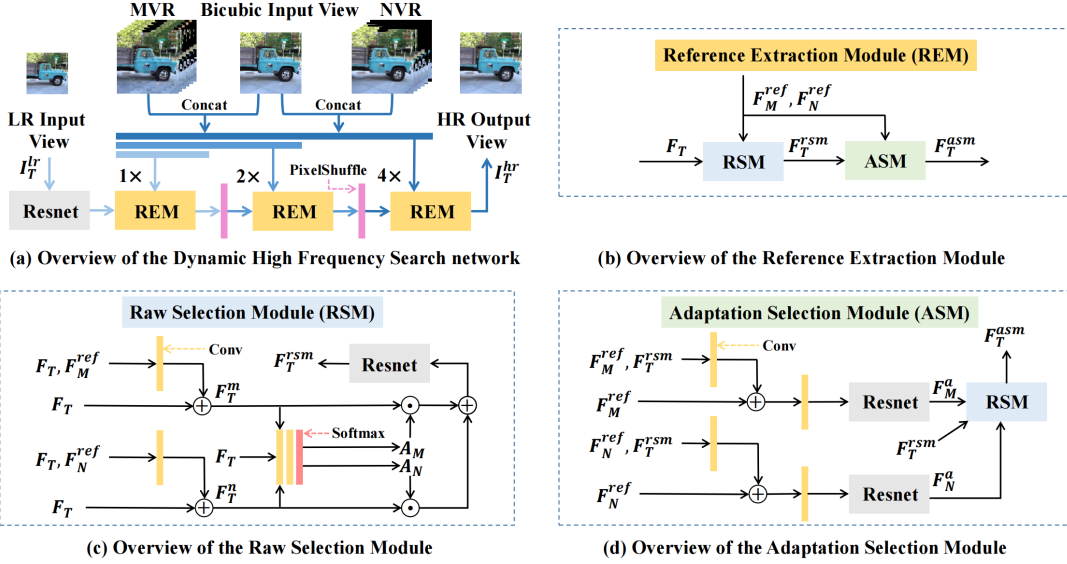


Figure 4: Overview of the proposed Dynamic High-Frequency Search (DHFS) network, which contains three Reference Extraction Module (REM). Each REM includes a Raw Selection Module (RSM) and an Adaptation Selection Module (ASM) to exploit the high-frequency textural details in reference images dynamically.

feature (F_M^{ref} and F_N^{ref}). On the other hand, we obtain the textural features F_T from LR input view using several residual layers. Then, we use three Reference Extraction Module (REM) that do not share parameters. Each REM includes a Raw Selection Module (RSM) and an Adaptation Selection Module (ASM) to exploit the high-frequency textural details in reference images dynamically, as shown in Figure 4(b). We adopt PixelShuffle [33] layer for up-sampling with factor 2.

Raw Selection Module. RSM first extracts high-frequency textural details as residues from MVR features (F_T, F_M^{ref}) and NVR features (F_T, F_M^{ref}), and adds them to the feature of the LR input view F_T , getting F_T^m and F_T^n respectively. Then, it aggregates them into the final output F_T^{rsm} via selection map A_m and A_n . Figure 4(c) shows this process, and the formula is as follows:

$$\begin{aligned} F_T^m &= F_T + \text{Conv}_1(F_T, F_M^{\text{ref}}) \\ F_T^n &= F_T + \text{Conv}_1(F_T, F_N^{\text{ref}}) \\ A_M, A_N &= \text{Softmax}(\text{Conv}_2(F_T^m, F_T^n, F_T)) \\ F_T^{\text{rsm}} &= \text{Resnet}(A_M F_T^m + A_N F_T^n). \end{aligned} \quad (5)$$

We find that RSM extracts more reference features from NVRs than from MVRs. Reference features are generated by the feature extractor rather than residual layers such as F_T , resulting in a feature difference between reference feature and F_T . Due to the feature difference, it is difficult for the network to extract high-frequency textural details from MVR features which contain numerous artifacts and alignment errors. However, MVRs contain rich high-frequency textural details that are extremely useful for reconstructing the high-quality SR output view. As a result, we propose using ASM to reduce feature difference and feature artifacts, increasing DHFS capabilities of extracting MVR high-frequency details.

Adaptation Selection Module. As shown in Figure 4(d), ASM first adds residues, calculated from $(F_M^{\text{ref}}, F_T^{\text{rsm}})$ and $(F_N^{\text{ref}}, F_T^{\text{rsm}})$, to F_M^{ref} and F_N^{ref} . Then, utilizing numerous residual layers, ASM adapts reference features to F_T^{rsm} , reducing the feature difference and artifact features in reference features. Finally, it takes the adapted reference feature (F_M^a and F_N^a) and F_T^{rsm} as the input of another RSM to extract high-frequency feature details. We define the process in ASM as follows:

$$\begin{aligned} F_M^a &= \text{Resnet}(\text{Conv}_2(F_M^{\text{ref}} + \text{Conv}_1(F_M^{\text{ref}}, F_T^{\text{rsm}}))) \\ F_N^a &= \text{Resnet}(\text{Conv}_2(F_N^{\text{ref}} + \text{Conv}_1(F_N^{\text{ref}}, F_T^{\text{rsm}}))) \\ F_T^{\text{asm}} &= \text{RSM}(F_M^a, F_N^a, F_T^{\text{rsm}}). \end{aligned} \quad (6)$$

As a result, dynamic extraction via RSM and ASM makes effective use of the HF textural details contained in the Refs.

3.4 Loss Functions

Similar to most SR models, we adopt the reconstruction loss \mathcal{L}_{rec} , adversarial loss \mathcal{L}_{adv} , and perceptual loss \mathcal{L}_{per} in our training stage. The \mathcal{L}_{adv} and \mathcal{L}_{per} are used to improve the visual quality, and we define the overall loss as follows:

$$\mathcal{L}_{\text{overall}} = \mathcal{L}_{\text{rec}} + \lambda_{\text{adv}} \mathcal{L}_{\text{adv}} + \lambda_{\text{per}} \mathcal{L}_{\text{per}} \quad (7)$$

Specifically, we employ ℓ_1 -norm for reconstruction loss and adopt the WGAN-GP [9] structure to obtain adversarial loss. For perceptual loss [14], it is calculated on the VGG19 [35] features of conv3-2, conv4-2, and conv5-2.

	Model	Train	Playground	M60	Truck	Total
SISR	EDSR [21]	28.05 / 0.8294 / 0.226	28.33 / 0.8070 / 0.318	31.38 / 0.9072 / 0.165	28.19 / 0.8535 / 0.209	28.99 / 0.8493 / 0.230
	RCAN [51]	28.56 / 0.8351 / 0.228	29.68 / 0.8117 / 0.320	32.41 / 0.9126 / 0.163	28.93 / 0.8583 / 0.213	29.89 / 0.8544 / 0.231
	HAN [27]	28.43 / 0.8321 / 0.222	29.59 / 0.8098 / 0.315	32.25 / 0.9103 / 0.167	28.77 / 0.8551 / 0.207	29.76 / 0.8518 / 0.228
	ESRGAN [41]	25.53 / 0.7512 / 0.109	25.48 / 0.6810 / 0.151	29.52 / 0.8666 / 0.091	26.00 / 0.7893 / 0.097	26.63 / 0.7720 / 0.112
	SPSR [25]	25.68 / 0.7495 / 0.106	26.61 / 0.6900 / 0.133	29.85 / 0.8631 / 0.087	26.49 / 0.7920 / 0.090	27.16 / 0.7736 / 0.104
VSR	RBPN [10]	28.35 / 0.8314 / 0.236	29.66 / 0.8131 / 0.321	32.23 / 0.9117 / 0.171	28.77 / 0.8563 / 0.217	29.75 / 0.8531 / 0.236
	RSDN [12]	27.68 / 0.8148 / 0.240	29.05 / 0.7954 / 0.314	31.05 / 0.8886 / 0.189	28.23 / 0.8402 / 0.218	29.00 / 0.8347 / 0.240
	MuCAN [18]	28.46 / 0.8363 / 0.215	29.66 / 0.8148 / 0.296	32.56 / 0.9175 / 0.150	28.90 / 0.8607 / 0.200	29.90 / 0.8573 / 0.215
	IconVSR [4]	28.31 / 0.8319 / 0.227	29.69 / 0.8172 / 0.310	32.36 / 0.9157 / 0.151	28.62 / 0.8538 / 0.218	29.75 / 0.8547 / 0.227
Ref-SR	TTSR [45]	26.28 / 0.7661 / 0.118	27.08 / 0.7129 / 0.155	29.97 / 0.8626 / 0.108	26.80 / 0.8016 / 0.115	27.53 / 0.7858 / 0.124
	TTSR-rec [45]	28.16 / 0.8277 / 0.227	29.32 / 0.8039 / 0.319	31.84 / 0.9060 / 0.162	28.51 / 0.8509 / 0.214	29.46 / 0.8471 / 0.231
	MASA [23]	25.48 / 0.7301 / 0.142	26.37 / 0.6822 / 0.152	28.89 / 0.8333 / 0.120	25.88 / 0.7722 / 0.121	26.66 / 0.7545 / 0.134
	MASA-rec [23]	28.43 / 0.8375 / 0.208	29.41 / 0.8073 / 0.309	32.10 / 0.9119 / 0.152	28.74 / 0.8586 / 0.205	29.67 / 0.8538 / 0.218
	C^2 -Matching [13]	28.13 / 0.8247 / 0.150	28.95 / 0.7844 / 0.210	31.71 / 0.9004 / 0.119	28.37 / 0.8441 / 0.151	29.29 / 0.8384 / 0.158
	C^2 -Matching-rec [13]	28.71 / 0.8473 / 0.201	29.62 / 0.8160 / 0.305	32.32 / 0.9155 / 0.147	28.92 / 0.8648 / 0.194	29.89 / 0.8609 / 0.212
	MVSRnet	27.57 / 0.8222 / 0.085	27.99 / 0.7694 / 0.104	31.73 / 0.9065 / 0.068	28.03 / 0.8505 / 0.082	28.83 / 0.8372 / 0.085
	MVSRnet-rec	29.04 / 0.8588 / 0.183	29.93 / 0.8371 / 0.275	32.88 / 0.9278 / 0.127	29.19 / 0.8757 / 0.178	30.26 / 0.8748 / 0.191

Table 1: Quantitative comparison on Tanks and Temples dataset. \uparrow PSNR / \uparrow SSIM / \downarrow LPIPS are used for evaluation. SISR, VSR, and Ref-SR methods are grouped separately. ESRGAN, SPSR, TTSR, MASA, C^2 -Matching, and MVSRnet are GAN-based methods and the best results are in bold.

	Model	BlendedMVS	GTAV
SISR	EDSR [21]	27.80 / 0.7198 / 0.393	30.93 / 0.8478 / 0.211
	RCAN [51]	27.90 / 0.7227 / 0.393	31.23 / 0.8530 / 0.212
	HAN [27]	27.86 / 0.7211 / 0.396	31.13 / 0.8515 / 0.206
	ESRGAN [41]	25.50 / 0.6315 / 0.173	28.26 / 0.7746 / 0.105
	SPSR [25]	25.72 / 0.6406 / 0.168	28.37 / 0.7739 / 0.102
VSR	RBPN [10]	27.79 / 0.7179 / 0.408	31.27 / 0.8559 / 0.218
	RSDN [12]	26.38 / 0.6412 / 0.480	30.26 / 0.8365 / 0.223
	MuCAN [18]	27.72 / 0.7162 / 0.400	31.24 / 0.8585 / 0.196
	IconVSR [4]	27.53 / 0.7089 / 0.408	31.41 / 0.8633 / 0.205
Ref-SR	TTSR [45]	26.09 / 0.6567 / 0.201	28.80 / 0.7914 / 0.121
	TTSR-rec [45]	27.68 / 0.7193 / 0.396	30.79 / 0.8485 / 0.216
	MASA [23]	25.84 / 0.6468 / 0.220	28.05 / 0.7699 / 0.131
	MASA-rec [23]	27.82 / 0.7335 / 0.375	31.12 / 0.8613 / 0.196
	C^2 -Matching [13]	27.24 / 0.7039 / 0.281	30.57 / 0.8396 / 0.153
	C^2 -Matching-rec [13]	27.99 / 0.7377 / 0.370	31.21 / 0.8628 / 0.194
	MVSRnet	26.90 / 0.7080 / 0.182	30.27 / 0.8462 / 0.085
	MVSRnet-rec	28.03 / 0.7457 / 0.360	31.60 / 0.8775 / 0.179

Table 2: Quantitative comparison on BlendedMVS and GTAV datasets. \uparrow PSNR / \uparrow SSIM / \downarrow LPIPS are used for evaluation. SISR, VSR, and Ref-SR methods are grouped separately.

4 EXPERIMENTS

4.1 Datasets and Training Details

Datasets. As the multi-view image super-resolution problem focuses on multi-view settings, we compare our MVSRnet to the state of the art on three challenging multi-view datasets: Tanks and Temples [15], BlendedMVS [47], and GTAV [11]. The real-world images captured in Tanks and Temples dataset and BlendedMVS are irregular distribution. GTAV is a photo-realistic synthetic dataset containing urban scenes captured in the video game Grand Theft Auto V. Specifically, we use 17 scenes from Tanks and Temples for training and 4 (Train, Playground, M60, and Truck) for testing, the same as [29]. In addition, the camera pose and the depth map we use are provided by [29] for Tanks and Temple. Additionally, we evaluate ten scenes in BlendedMVS and all scenes in GTAV, proving

the generalization capacity of our MVSRnet. The number of views in each scene of the Tanks and Temples and BlendedMVS datasets is concentrated in 300-400 and 60-150, and the GTAV dataset is 100. We set the SR factor as $\times 4$, and we generate LR multi-view images and depth maps by bicubic and modify the camera intrinsic matrices according to the SR factor.

Training Details. We first utilize the Geometry-Aware Reference Synthesis module to synthesize MVRs and NVRs for each LR input view. Specifically, we synthesize V MVRs and V NVRs from all LR multi-view images and L adjacent views, respectively. V is equal to 6, and we empirically set the L to 6. Then, we use synthesized reference images and the LR input view to train the Dynamic High-Frequency Search network from scratch on an Nvidia GeForce RTX 3090 GPU. We implement our method in Pytorch, and the total number of training iterations is 200,000, with a batch size of 2 and a LR patch size of 80×160 pixels. In addition, we decay the learning rate from $1e-4$ to $1e-7$ in a cosine annealing way, and we choose ADAM with parameters $\beta_1 = 0.9$, and $\beta_2 = 0.999$ as optimizer. We set λ_{adv} and λ_{per} in Eq.(7) to $5e-3$ and $1e-2$.

4.2 Comparison with State-of-the-Art Methods

We compare our MVSRnet with recent SISR, VSR, and Ref-SR methods. We use five SISR methods, including EDSR [21], RCAN [51], HAN [27], ESRGAN [41], and SPSR [25], four VSR methods, including RBPN [10], RSDN [12], MuCAN [18], and IconVSR [4], and three Ref-SR methods, including TTSR [45], MASA [23], and C^2 -Matching [13]. We use the best results from their pre-trained and fine-tuned models using our Tanks and Temples dataset for display. Because RSDN and MuCAN do not supply training code, we rely on the pre-trained models they provide. We employ an MVR synthesized from the top-1 HF index maps as the input to Ref-SR methods because these methods are incapable of processing hundreds of reference images. Our compared Ref-SR methods may concatenate the references in a row or column to conduct multi-reference SR,

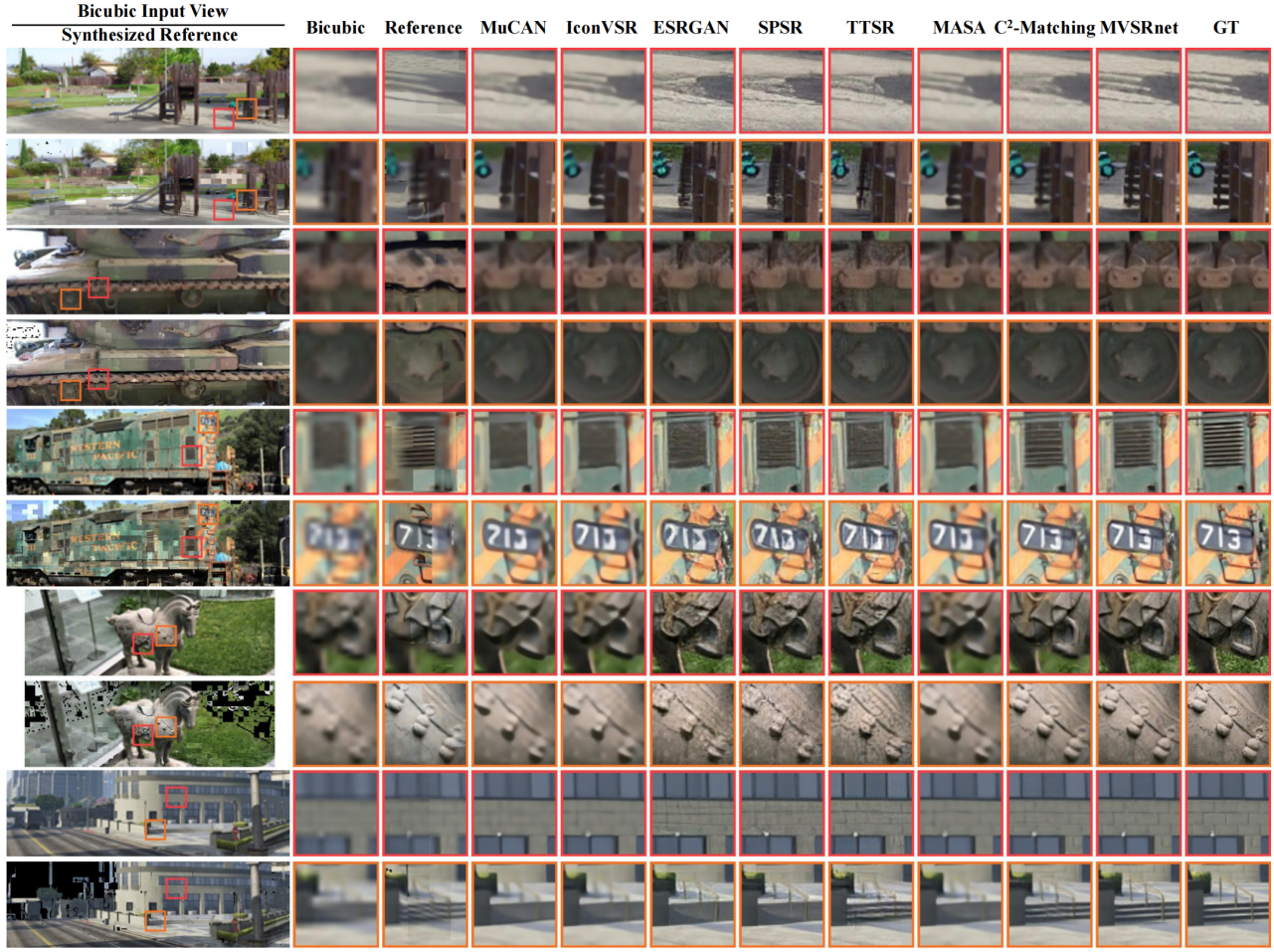


Figure 5: Qualitative comparisons. The top three examples are Playground, M60, and Train scene in Tanks and Temple dataset. The fourth and fifth example come from BlendedMVS and GTAV datasets, respectively. Zoom in for better visualization.

but the GPU runs out of memory when employing two synthesized references. ESRGAN, SPSR, TTSR, MASA, and C^2 -Matching are all GAN-based models, whereas the remaining models rely solely on reconstruction loss. To ensure a fair comparison, we train our model with overall loss (Eq.(7)) and solely reconstruction loss and refer to them as MVSRnet and MVSRnet-rec, respectively.

Quantitative Comparison. Table 1 presents the quantitative results of the Tanks and Temples dataset. In Table 2, we also verify the generalization capacity of our MVSRnet using BlendedMVS and GTAV, and our approach continues to perform the best. The PSNR of GAN-based C^2 -Matching in Table 1 and Table 2 is higher than our MVSRnet, while MVSRnet reduces the LPIPS [49] error by around 35%-46% when compared to C^2 -Matching. LPIPS is validated to human perception and is commonly used as a metric for evaluating GAN-based models. While our LPIPS is comparable to that of SPSR in BlendedMVS, our PSNR and SSIM are 1.18dB and 0.0674 higher, respectively. In summary, our proposed method outperforms the state of the art by a significant margin.

Qualitative Evaluation. The visual results shown in Figure 5 reveal that our method is capable of producing finer details, and they lead to two conclusions. (a) Our reference image generated from all LR multi-view images is more beneficial for SR than the image self-reference (SISR) and adjacent views (VSR). For example, the reference image of the fourth example contains more realistic horse details than the bicubic input view. Thus, using our reference image, MVSRnet generates more fine textural details of the horse when compared to SISR methods (ESRGAN and SPSR) and VSR methods (MuCAN and IconVSR). (b) Our DHFS network, including RSM and ASM, shows its effectiveness and robustness in identifying and extracting useful features from the reference images. Specifically, because our synthesized reference image is used as an input, Ref-SR methods such as TTSR, MASA, and C^2 -Matching can produce textural results. They are, however, not robust to artifacts in the synthesized reference. For example, in Figure 5, the reference image of the third example contains blur artifacts, resulting in more blur areas in the C^2 -Matching image than in our MVSRnet image.

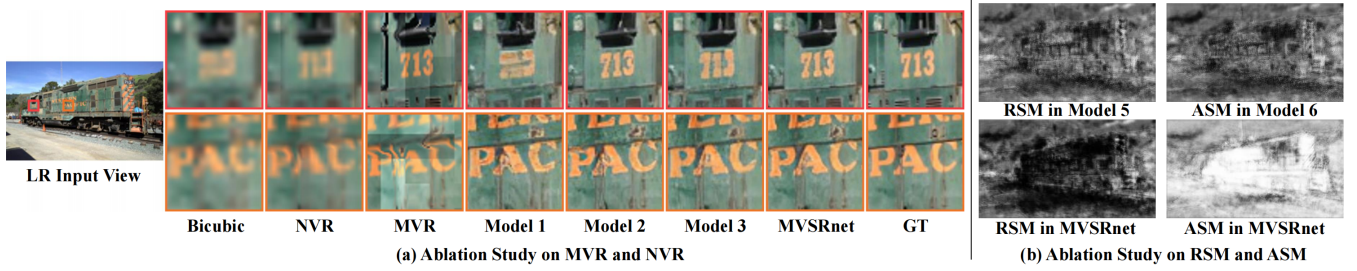


Figure 6: Ablation study. (a) Effectiveness of MVR and NVR. Model 1 uses neither MVR nor NVR, and Model 2 and 3 only use MVR or NVR. (b) Effectiveness of RSM and ASM. The upper left and upper right are the selection map A_M of features F_T^M from RSM in Model 5 and from ASM in Model 6, respectively. The lower left and lower right are the selection map A_M from RSM and from ASM in MVSNet.

4.3 Ablation Study

Muti-View Reference Image (MVR) and Near-View Reference Image (NVR). We analyze the MVR and NVR that have complementary effects on SR tasks. The ablation Model 1 does not input both MVR and NVR, and Model 2 and Model 3 do not input NVR and MVR, respectively. As illustrated in Figure 6(a), MVR contains high-frequency details (sharp number ‘713’) as well as noticeable artifacts (the incorrect structure of letter ‘PAC’). In contrast, NVR has fewer artifacts and details of ‘PAC’ and ‘713’ than MVR, but there are still more high-frequency details than the bicubic input view. We discover that MVSNet recovers the exact number ‘713’ than Model 3 and produces fewer ‘PAC’ artifacts than Model 2. Additionally, we conduct quantitative ablation study, and Table 3 reveals that MVSNet has superior PSNR performance than Model 2 and Model 3 by 0.38dB and 0.45 dB, respectively. These experiments fully demonstrate the complementary effects of MVR and NVR.

In addition, we search for the optimal number V of MVR and NVR. The LR details and artifacts areas grow in relation to the number V of reference images, making it challenging for the network to identify and extract relevant high frequencies details. We perform ablation studies with V to 1, 2, 4, 6, and 8, and we achieve the best performance when we set V to 6, as shown in Table 4. We also conduct an ablation study on the hyper-parameter of patch size ps as 4/8/16/32/64 in GARS module, and achieve the best performance when we set ps to 16, as shown in Table 4. The reason is that when the patch size is too small, there are numerous selection mistakes and block-boundary artifacts in the synthesized reference image. When the block size is too large, the selected patches are blurry and lack a significant amount of high-frequency texture details.

Raw Selection Module (RSM) and Adaptation Selection Module (ASM). The ablation Model 4 does not include both RSM and ASM, and Model 5 and Model 6 do not include ASM and RSM, respectively. Figure 6(b) shows that selected areas (denoted as white) in the selection map of ‘ASM in MVSNet’ are more than ‘RSM in Model 5’ and ‘ASM in Model 6’, indicating that more MVR HR feature details are selected for SR. This is because a small difference between features can help the network identify and extract useful features. As mentioned in Section 3.3, ASM implicitly decreases the difference between reference features and input view features and reduces artifact features in reference features, making it easier for the network to extract useful features in MVR. RSM, on the

Model	MVR	NVR	RSM	ASM	Parameters	Tanks and Temple
Model 1			✓	✓	19.51M	27.33 / 0.7734 / 0.108
Model 2	✓		✓	✓	19.56M	28.45 / 0.8215 / 0.089
Model 3		✓	✓	✓	19.56M	28.38 / 0.8182 / 0.089
Model 4	✓	✓			19.73M	28.68 / 0.8323 / 0.085
Model 5	✓	✓	✓		19.62M	28.71 / 0.8324 / 0.084
Model 6	✓	✓		✓	19.46M	28.72 / 0.8340 / 0.083
MVSNet	✓	✓	✓	✓	19.42M	28.83 / 0.8372 / 0.085

Table 3: Quantitative ablation study on the MVR and NVR and quantitative ablation study on the RSM and ASM.

V	Tanks & Temple	Patch Size	Tanks & Temple
1	28.49 / 0.8252 / 0.087	4	28.72 / 0.8335 / 0.082
2	28.73 / 0.8353 / 0.085	8	28.76 / 0.8336 / 0.084
4	28.71 / 0.8334 / 0.085	16	28.83 / 0.8372 / 0.085
6	28.83 / 0.8372 / 0.085	32	28.73 / 0.8323 / 0.086
8	28.56 / 0.8289 / 0.087	64	28.56 / 0.8273 / 0.087

Table 4: Columns 1 and 2: ablation study of the optimal number V of MVR and V NVR. Columns 3 and 4: ablation study of the patch size ps in GARS module.

other hand, uses a residual process to adapt input view features to reference features, as indicated in Eq.(5). The different ways ASM and RSM incorporate features makes feature extraction more sufficient. Thus, combining RSM and ASM significantly improves the power of DHFS to extract and identify HF details when compared to using only RSM or ASM. We also verify them using the quantitative evaluation displayed in Table 3. MVSNet improves the PSNR value by 0.12dB and 0.11dB, respectively, when compared to Model 5 and 6, demonstrating the usefulness of using both RSM and ASM.

5 CONCLUSION

We propose the MVSNet for multi-view image super-resolution that aims to super-resolve each view by utilizing all views as references. Our Geometry-Aware Reference Synthesis module, in particular, can synthesize reference images from all LR multi-view images by explicitly using geometry information. The reference image contains high-frequency details and is aligned with the input view. Then we implement a Dynamic High-Frequency Search

network which includes the Raw Selection Module and Adaptation Selection Module, to dynamically select useful features in the synthesized reference features for super-resolution. We have achieved best experimental results compared with state-of-the-art methods and this work enriches the Reference-Based SR research.

REFERENCES

- [1] Leif Berg and Judy Vance. 2017. Industry use of virtual reality in product design and manufacturing: a survey. *Virtual Reality* 21 (03 2017). <https://doi.org/10.1007/s10055-016-0293-9>
- [2] Tom E. Bishop, Sara Zanetti, and Paolo Favaro. 2009. Light field superresolution. In *2009 IEEE International Conference on Computational Photography (ICCP)*. 1–9. <https://doi.org/10.1109/ICCPHOT.2009.5559010>
- [3] F.P. Brooks. 1999. What's real about virtual reality? *IEEE Computer Graphics and Applications* 19, 6 (1999), 16–27. <https://doi.org/10.1109/38.799723>
- [4] Kelvin C.K. Chan, Xintao Wang, Ke Yu, Chao Dong, and Chen Change Loy. 2021. BasicVSR: The Search for Essential Components in Video Super-Resolution and Beyond. In *Proceedings of the IEEE/CVF Conference on Computer Vision and Pattern Recognition (CVPR)*. 4947–4956.
- [5] Jifeng Dai, Haozhi Qi, Yuwen Xiong, Yi Li, Guodong Zhang, Han Hu, and Yichen Wei. 2017. Deformable Convolutional Networks. In *Proceedings of the IEEE International Conference on Computer Vision (ICCV)*.
- [6] Chao Dong, Chen Change Loy, Kaiming He, and Xiaou Tang. 2016. Image Super-Resolution Using Deep Convolutional Networks. *IEEE Transactions on Pattern Analysis and Machine Intelligence* 38, 2 (2016), 295–307. <https://doi.org/10.1109/TPAMI.2015.2439281>
- [7] Bastian Goldluecke and Daniel Cremers. 2009. Superresolution texture maps for multiview reconstruction. In *2009 IEEE 12th International Conference on Computer Vision*. 1677–1684. <https://doi.org/10.1109/ICCV.2009.5459378>
- [8] Ian J. Goodfellow, Jean Pouget-Abadie, Mehdi Mirza, Bing Xu, David Warde-Farley, Sherjil Ozair, Aaron C. Courville, and Yoshua Bengio. 2014. Generative Adversarial Nets. In *NIPS*. 2672–2680.
- [9] Ishaan Gulrajani, Faruk Ahmed, Martin Arjovsky, Vincent Dumoulin, and Aaron C. Courville. 2017. Improved Training of Wasserstein GANs. In *NIPS*. 5769–5779. <http://papers.nips.cc/paper/7159-improved-training-of-wasserstein-gans.pdf>
- [10] Muhammad Haris, Gregory Shakhnarovich, and Norimichi Ukita. 2019. Recurrent Back-Projection Network for Video Super-Resolution. In *Proceedings of the IEEE/CVF Conference on Computer Vision and Pattern Recognition (CVPR)*.
- [11] Po-Han Huang, Kevin Matzen, Johannes Kopf, Narendra Ahuja, and Jia-Bin Huang. 2018. DeepMVS: Learning Multi-View Stereopsis. In *Proceedings of the IEEE Conference on Computer Vision and Pattern Recognition (CVPR)*.
- [12] Takashi Isobe, Xu Jia, Shuhang Gu, Songjiang Li, Shengjin Wang, and Qi Tian. 2020. Video Super-Resolution with Recurrent Structure-Detail Network. In *Computer Vision – ECCV 2020*. Cham, 645–660.
- [13] Yuming Jiang, Kelvin C.K. Chan, Xintao Wang, Chen Change Loy, and Ziwei Liu. 2021. Robust Reference-Based Super-Resolution via C2-Matching. In *Proceedings of the IEEE/CVF Conference on Computer Vision and Pattern Recognition (CVPR)*. 2103–2112.
- [14] Justin Johnson, Alexandre Alahi, and Li Fei-Fei. 2016. Perceptual Losses for Real-Time Style Transfer and Super-Resolution. In *Computer Vision – ECCV 2016*. Cham, 694–711.
- [15] Arno Knapitsch, Jaesik Park, Qian-Yi Zhou, and Vladlen Koltun. 2017. Tanks and temples: benchmarking large-scale scene reconstruction. *ACM Trans. Graph.* 36, 4 (2017), 78:1–78:13.
- [16] Christian Ledig, Lucas Theis, Ferenc Huszar, Jose Caballero, Andrew Cunningham, Alejandro Acosta, Andrew Aitken, Alykhan Tejani, Johannes Totz, Zehan Wang, and Wenzhe Shi. 2017. Photo-Realistic Single Image Super-Resolution Using a Generative Adversarial Network. In *Proceedings of the IEEE Conference on Computer Vision and Pattern Recognition (CVPR)*.
- [17] Chuen-Chien Lee, Ali Tabatabai, and Kenji Tashiro. 2015. Free viewpoint video (FVV) survey and future research direction. *APSIPA Transactions on Signal and Information Processing* 4 (2015), e15. <https://doi.org/10.1017/ATSP.2015.18>
- [18] Wenbo Li, Xin Tao, Tairan Guo, Lu Qi, Jiangbo Lu, and Jiaya Jia. 2020. MuCAN: Multi-correspondence Aggregation Network for Video Super-Resolution. In *Computer Vision – ECCV 2020*. Cham, 335–351.
- [19] Yawei Li, Xiaofeng Li, Zhizhong Fu, and Wenli Zhong. 2016. Multiview Video Super-Resolution via Information Extraction and Merging. In *Proceedings of the 24th ACM International Conference on Multimedia (Amsterdam, The Netherlands) (MM '16)*. New York, NY, USA, 446–450. <https://doi.org/10.1145/2964284.2967260>
- [20] Yawei Li, Vagia Tsiminaki, Radu Timofte, Marc Pollefeys, and Luc Van Gool. 2019. 3D Appearance Super-Resolution With Deep Learning. In *Proceedings of the IEEE/CVF Conference on Computer Vision and Pattern Recognition (CVPR)*.
- [21] Bee Lim, Sanghyun Son, Heewon Kim, Seungjun Nah, and Kyoung Mu Lee. 2017. Enhanced Deep Residual Networks for Single Image Super-Resolution. In *The IEEE Conference on Computer Vision and Pattern Recognition (CVPR) Workshops*.
- [22] D.G. Lowe. 1999. Object recognition from local scale-invariant features. In *Proceedings of the Seventh IEEE International Conference on Computer Vision*, Vol. 2. 1150–1157 vol.2. <https://doi.org/10.1109/ICCV.1999.790410>
- [23] Liying Lu, Wenbo Li, Xin Tao, Jiangbo Lu, and Jiaya Jia. 2021. MASA-SR: Matching Acceleration and Spatial Adaptation for Reference-Based Image Super-Resolution. In *Proceedings of the IEEE/CVF Conference on Computer Vision and Pattern Recognition (CVPR)*. 6368–6377.
- [24] Shao-Ping Lu, Sen-Mao Li, Rong Wang, Gauthier Lafruit, Ming-Ming Cheng, and Adrian Munteanu. 2021. Low-Rank Constrained Super-Resolution for Mixed-Resolution Multiview Video. *IEEE Transactions on Image Processing* 30 (2021), 1072–1085. <https://doi.org/10.1109/TIP.2020.3042064>
- [25] Cheng Ma, Yongming Rao, Yan Cheng, Ce Chen, Jiwen Lu, and Jie Zhou. 2020. Structure-Preserving Super Resolution With Gradient Guidance. In *Proceedings of the IEEE/CVF Conference on Computer Vision and Pattern Recognition (CVPR)*.
- [26] Leonard McMillan. 1997. *An image-based approach to three-dimensional computer graphics*. Ph. D. Dissertation. Citeseer.
- [27] Ben Niu, Weilei Wen, Wenqi Ren, Xiangde Zhang, Lianping Yang, Shuzhen Wang, Kaihao Zhang, Xiaochun Cao, and Haifeng Shen. 2020. Single Image Super-Resolution via a Holistic Attention Network. In *Computer Vision – ECCV 2020*. 191–207.
- [28] Audrey Richard, Ian Cherabier, Martin R. Oswald, Vagia Tsiminaki, Marc Pollefeys, and Konrad Schindler. 2019. Learned Multi-View Texture Super-Resolution. In *2019 International Conference on 3D Vision (3DV)*. 533–543. <https://doi.org/10.1109/3DV.2019.00065>
- [29] Gernot Riegler and Vladlen Koltun. 2020. Free View Synthesis. In *European Conference on Computer Vision*.
- [30] Gernot Riegler and Vladlen Koltun. 2021. Stable View Synthesis. In *Proceedings of the IEEE/CVF Conference on Computer Vision and Pattern Recognition (CVPR)*. 12216–12225.
- [31] Johannes L. Schonberger and Jan-Michael Frahm. 2016. Structure-From-Motion Revisited. In *Proceedings of the IEEE Conference on Computer Vision and Pattern Recognition (CVPR)*.
- [32] Johannes L. Schonberger, Enliang Zheng, Jan-Michael Frahm, and Marc Pollefeys. 2016. Pixelwise View Selection for Unstructured Multi-View Stereo. In *Computer Vision – ECCV 2016*. Cham, 501–518.
- [33] Wenzhe Shi, Jose Caballero, Ferenc Huszar, Johannes Totz, Andrew P. Aitken, Rob Bishop, Daniel Rueckert, and Zehan Wang. 2016. Real-Time Single Image and Video Super-Resolution Using an Efficient Sub-Pixel Convolutional Neural Network. In *Proceedings of the IEEE Conference on Computer Vision and Pattern Recognition (CVPR)*.
- [34] Gyumin Shim, Jinsun Park, and In So Kweon. 2020. Robust Reference-Based Super-Resolution With Similarity-Aware Deformable Convolution. In *Proceedings of the IEEE/CVF Conference on Computer Vision and Pattern Recognition (CVPR)*.
- [35] Karen Simonyan and Andrew Zisserman. 2015. Very Deep Convolutional Networks for Large-Scale Image Recognition. In *International Conference on Learning Representations*.
- [36] Aljoscha Smolic, Karsten Mueller, Philipp Merkle, Christoph Fehn, Peter Kauff, Peter Eisert, and Thomas Wiegand. 2006. 3D Video and Free Viewpoint Video - Technologies, Applications and MPEG Standards. In *2006 IEEE International Conference on Multimedia and Expo*. 2161–2164. <https://doi.org/10.1109/ICME.2006.262683>
- [37] Yuqi Sun, Ri Cheng, Bo Yan, and Shili Zhou. 2021. Space-Angle Super-Resolution for Multi-View Images. In *MM '21: ACM Multimedia Conference, Virtual Event, China, October 20 - 24, 2021*. ACM, 750–759. <https://doi.org/10.1145/3474085.3475244>
- [38] Vagia Tsiminaki, Jean-Sebastien Franco, and Edmond Boyer. 2014. High Resolution 3D Shape Texture from Multiple Videos. In *Proceedings of the IEEE Conference on Computer Vision and Pattern Recognition (CVPR)*.
- [39] Ashish Vaswani, Noam Shazeer, Niki Parmar, Jakob Uszkoreit, Llion Jones, Aidan N Gomez, Łukasz Kaiser, and Illia Polosukhin. 2017. Attention is All you Need. In *Advances in Neural Information Processing Systems*, Vol. 30.
- [40] Longguang Wang, Yingqian Wang, Zhengfa Liang, Zaiping Lin, Jungang Yang, Wei An, and Yulan Guo. 2019. Learning Parallax Attention for Stereo Image Super-Resolution. In *Proceedings of the IEEE/CVF Conference on Computer Vision and Pattern Recognition (CVPR)*.
- [41] Xintao Wang, Ku Yu, Shixiang Wu, Jinjin Gu, Yihao Liu, Chao Dong, Yu Qiao, and Chen Change Loy. 2018. ESRGAN: Enhanced Super-Resolution Generative Adversarial Networks. In *Proceedings of the European Conference on Computer Vision (ECCV) Workshops*.
- [42] Yingqian Wang, Longguang Wang, Jungang Yang, Wei An, Jingyi Yu, and Yulan Guo. 2020. Spatial-Angular Interaction for Light Field Image Super-Resolution. In *Computer Vision – ECCV 2020*. 290–308.
- [43] Sven Wanner and Bastian Goldluecke. 2014. Variational Light Field Analysis for Disparity Estimation and Super-Resolution. *IEEE Transactions on Pattern Analysis and Machine Intelligence* 36, 3 (2014), 606–619. <https://doi.org/10.1109/TPAMI.2013.147>
- [44] Xu Yan, Weibing Zhao, Kun Yuan, Ruimao Zhang, Zhen Li, and Shuguang Cui. 2020. Towards Content-Independent Multi-Reference Super-Resolution: Adaptive

Pattern Matching and Feature Aggregation. In *Computer Vision – ECCV 2020*. 52–68.

[45] Fuzhi Yang, Huan Yang, Jianlong Fu, Hongtao Lu, and Baining Guo. 2020. Learning Texture Transformer Network for Image Super-Resolution. In *Proceedings of the IEEE/CVF Conference on Computer Vision and Pattern Recognition (CVPR)*.

[46] Yao Yao, Zixin Luo, Shiwei Li, Tian Fang, and Long Quan. 2018. MVSNet: Depth Inference for Unstructured Multi-view Stereo. In *Proceedings of the European Conference on Computer Vision (ECCV)*.

[47] Yao Yao, Zixin Luo, Shiwei Li, Jingyang Zhang, Yufan Ren, Lei Zhou, Tian Fang, and Long Quan. 2020. BlendedMVS: A Large-Scale Dataset for Generalized Multi-View Stereo Networks. In *Proceedings of the IEEE/CVF Conference on Computer Vision and Pattern Recognition (CVPR)*.

[48] Xinyi Ying, Yingqian Wang, Longguang Wang, Weidong Sheng, Wei An, and Yulan Guo. 2020. A Stereo Attention Module for Stereo Image Super-Resolution. *IEEE Signal Processing Letters* 27 (2020), 496–500. <https://doi.org/10.1109/LSP.2020.2973813>

[49] Richard Zhang, Phillip Isola, Alexei A. Efros, Eli Shechtman, and Oliver Wang. 2018. The Unreasonable Effectiveness of Deep Features as a Perceptual Metric. In *Proceedings of the IEEE Conference on Computer Vision and Pattern Recognition (CVPR)*.

[50] Shuo Zhang, Youfang Lin, and Hao Sheng. 2019. Residual Networks for Light Field Image Super-Resolution. In *Proceedings of the IEEE/CVF Conference on Computer Vision and Pattern Recognition (CVPR)*.

[51] Yulun Zhang, Kunpeng Li, Kai Li, Lichen Wang, Bineng Zhong, and Yun Fu. 2018. Image Super-Resolution Using Very Deep Residual Channel Attention Networks. In *ECCV*.

[52] Zhifei Zhang, Zhaowen Wang, Zhe Lin, and Hairong Qi. 2019. Image Super-Resolution by Neural Texture Transfer. In *Proceedings of the IEEE/CVF Conference on Computer Vision and Pattern Recognition (CVPR)*.

[53] Haitian Zheng, Mengqi Ji, Haoqian Wang, Yebin Liu, and Lu Fang. 2018. CrossNet: An End-to-end Reference-based Super Resolution Network using Cross-scale Warping. In *Proceedings of the European Conference on Computer Vision (ECCV)*.

[54] Xizhou Zhu, Han Hu, Stephen Lin, and Jifeng Dai. 2019. Deformable ConvNets V2: More Deformable, Better Results. In *Proceedings of the IEEE/CVF Conference on Computer Vision and Pattern Recognition (CVPR)*.

A LOSS FUNCTIONS

Reconstruction Loss. The ℓ_1 -norm of the reconstruction loss is used as follows:

$$\mathcal{L}_{\text{rec}} = \left\| I_T^{hr} - I_T^{gt} \right\|_1, \quad (8)$$

where I_T^{hr} and I_T^{gt} represent the output of our MVSNet and the high-resolution (HR) view of the ground truth, respectively.

Adversarial Loss. We use the WGAN-GP [9] structure to obtain adversarial loss [8]. WGAN-GP replaces the weight clipping with a gradient norm penalty to achieve stable training and generate high-quality samples. We define adversarial loss as follows:

$$\begin{aligned} \mathcal{L}_D = & \mathbb{E}_{I_T^{hr}} [D(I_T^{hr})] - \mathbb{E}_{I_T^{gt}} [D(I_T^{gt})] + \\ & \lambda \mathbb{E}_{\hat{I}} \left[\left(\left\| \nabla_{\hat{I}} D(\hat{I}) \right\|_2 - 1 \right)^2 \right], \end{aligned} \quad (9)$$

$$\mathcal{L}_G = -\mathbb{E}_{I_T^{hr}} [D(I_T^{hr})]. \quad (10)$$

where \hat{I} is the random sample of our network output I_T^{hr} and ground truth I_T^{gt} through combination, $(\hat{I} \leftarrow \epsilon I_T^{gt} + (1 - \epsilon) I_T^{hr}, \epsilon \sim U[0, 1])$.

Perceptual Loss. We utilize perceptual loss [14] to generate the photo-realistic image, which we define as follows:

$$L_{\text{per}} = \left\| \phi_i \left(I_T^{hr} \right) - \phi_i \left(I_T^{gt} \right) \right\|_1, \quad (11)$$

where ϕ_i denotes the i -th layer feature map of VGG19 [35], and we use the features of conv3-2, conv4-2, and conv5-2 to calculate the perceptual loss.

Table 5: Comparison to multi-view super-resolution method.

Model	Tanks and Temple	BlendedMVS
SASRnet [37]	28.99 / 0.8493 / 0.230	27.80 / 0.7198 / 0.393
MVSNet-rec	30.26 / 0.8748 / 0.191	28.03 / 0.7457 / 0.360

B COMPARE TO MULTI-VIEW SUPER-RESOLUTION METHOD

As far as we know, our MVSNet is the first to solve the multi-view image super-resolution problem using low-resolution images. Existing multi-view SR related methods rarely consider this problem. Some methods focus on multi-view texture [28] or light field images [50] and some other methods [19, 24] require high-resolution multi-view as a reference, which is not easily available in practice due to high storage costs and bandwidth constraints. The most similar method to ours is SASRnet [37]. It uses two adjacent low-resolution views to generate high-resolution source views and a novel view. In Tanks and Temples and BlendedMVS dataset, they have a source view PSNR of 29.29dB and 27.27dB, respectively, which is much lower than our 30.26dB and 28.03dB as shown in Table 5. Moreover, SASRnet fails in GTAV and generate dark images because their depth prediction module is sensitive to depth scale.

C NETWORK STRUCTURES

We illustrate the network structure of the Dynamic High-Frequency Search network in Table 6. It first uses a feature extractor to extract the features of multi-view reference images and near-view reference images at $1\times$, $2\times$, and $4\times$ scales, respectively. Then three Raw Selection Modules (RSM) and three Adaptation Selection Modules (ASM) are used to select the useful features from the reference features of different scales. We adopt the same structure as [13] for the discriminator.

D MODEL SIZE

This section compares the number of training parameters in Table 7. We provide two models, MVSNet-light and MVSNet-light-rec, for comparing model parameters. Specifically, for MVSNet-light, we reduce the number of channels in the feature extractor and residual layer to half and add three more residual layers to feature extractor. We also include the parameter of the discriminator in the total parameters for the GAN-based model. As shown in Table 7, the parameters of MVSNet-light-rec are only 0.36M more than MASA-rec, but our PSNR is 0.45dB, 0.18dB, and 0.33dB more than MASA-rec in Tanks and Temple, BlendedMVS, and GTAV, respectively. In summary, MVSNet-light not only has fewer parameters, but achieves better results than the state of the arts to a large extent.

E MORE VISUAL COMPARISON

In this section, we provide more visual comparisons with SISR methods (RCAN [51], ESRGAN [41], and SPSR [25]), VSR methods (MuCAN [18] and IconVSR [4]), and Ref-SR methods (TTSR [45] and C^2 -Matching [13]). Specifically, RCAN, MuCAN, IconVSR, and our MVSNet-rec only use the reconstruction loss, and ESRGAN, SPSR, TTSR, C^2 -Matching, and our MVSNet are all GAN-based models. The visual comparison of Tanks and Temple, BlendedMVS, and GTAV are shown in Figure 7 and Figure 8, Figure 9, and Figure 10, respectively.

F LIMITATION

We have two major limitations. First, we assume static sceneries like in most multi-view work [29, 30], and the denser the input views, the better the scene geometry estimation. As a result, we will concentrate on the MVISR task of dynamic scenes and design a strategy for dealing with situations in which there are just a few multi-view images accessible. Second, we preprocess all LR multi-view images to create synthesized reference images, so an elaborated online reference selection approach should be proposed.

Table 6: The network structure of our Dynamic High-Frequency Search network. MVR, NVR, and Bic denote the multi-view reference image, near-view reference image, and the bicubic of the LR input view, respectively. We present the convolution layer as $\text{Conv}(\text{input channels}, \text{output channels}, \text{kernel size}, \text{stride}, \text{padding})$. $RB \times N$ is a residual block with N residual layers, and we adopt the residual layer with channel attention described in [51]. In addition, we use PixelShuffle to upsample, and use ReLU in RB and LeakyReLU other places.

	Id	Layer Name		Id	Layer Name		Id	Layer Name		Id	Layer Name
Feature Extractor	1-0	Concat (MVRs, Bic)	RSM (scale 1x)	2-0	LR Input View	RSM (scale 2x)			RSM (scale 4x)		
	1-1	Conv(19,64,3,1,1), RB \times 3		2-1	Conv(3,64,3,1,1), RB \times 10						
	1-2	Conv(64,128,4,2,1), RB \times 3		2-2	Concat(\$2-1, \$1-3), Conv(320,64,3,1,1)		3-0	Concat(\$2-18, \$1-2), Conv(192,64,3,1,1)		4-0	Concat(\$3-16, \$1-1), Conv(128,64,3,1,1)
	1-3	Conv(128,256,4,2,1), RB \times 3		2-3	\$2-1+\$2-2		3-1	\$2-18+\$3-0		4-1	\$3-16+\$4-0
	1-4	Concat (NVRs, Bic)		2-4	Concat(\$2-1, \$1-7), Conv(320,64,3,1,1)		3-2	Concat(\$2-18, \$1-6), Conv(192,64,3,1,1)		4-2	Concat(\$3-16, \$1-5), Conv(128,64,3,1,1)
	1-5	Conv(19,64,3,1,1), RB \times 3		2-5	\$2-1+\$2-4		3-3	\$2-18+\$3-2		4-3	\$3-16+\$4-2
	1-6	Conv(64,128,4,2,1), RB \times 3		2-6	Concat(\$2-3, \$2-5, \$2-1), Conv(192,64,3,1,1), LeakyReLU, Conv(64,2,3,1,1), Softmax		3-4	Concat(\$3-1, \$3-3, \$2-18), Conv(192,64,3,1,1), LeakyReLU, Conv(64,2,3,1,1), Softmax		4-4	Concat(\$4-1, \$4-3, \$3-16), Conv(192,64,3,1,1), LeakyReLU, Conv(64,2,3,1,1), Softmax
	1-7	Conv(128,256,4,2,1), RB \times 3		2-7	\$2-3\times\$2-6[0]+\$2-5\times\$2-6[1], RB \times 8		3-5	\$3-1\times\$3-4[0]+\$3-3\times\$3-4[1], RB \times 6		4-5	\$4-1\times\$4-4[0]+\$4-3\times\$4-4[1], RB \times 4
ASMF	ASM (scale 1x)	ASM (scale 2x)	ASM (scale 4x)	2-8	Concat(\$1-3, \$2-7), Conv(320,256,3,1,1)		3-6	Concat(\$1-2, \$3-5), Conv(192,128,3,1,1)		4-6	Concat(\$1-1, \$4-5), Conv(128,64,3,1,1)
				2-9	\$1-3\times\$2-8, Conv(256,64,3,1,1), RB \times 8		3-7	\$1-2\times\$3-6, Conv(128,64,3,1,1), RB \times 6		4-7	\$1-1\times\$4-6, Conv(64,64,3,1,1), RB \times 4
				2-10	Concat(\$1-7, \$2-7), Conv(320,256,3,1,1)		3-8	Concat(\$1-6, \$3-5), Conv(192,128,3,1,1)		4-8	Concat(\$1-5, \$4-5), Conv(64,64,3,1,1)
				2-11	\$1-7\times\$2-10, Conv(256,64,3,1,1), RB \times 8		3-9	\$1-6\times\$3-8, Conv(128,64,3,1,1), RB \times 6		4-9	\$1-5\times\$4-8, Conv(64,64,3,1,1), RB \times 4
				2-12	Concat(\$2-7, \$2-9), Conv(128,64,3,1,1)		3-10	Concat(\$3-5, \$3-7), Conv(128,64,3,1,1)		4-10	Concat(\$4-5, \$4-7), Conv(128,64,3,1,1)
				2-13	\$2-7\times\$2-12		3-11	\$3-5\times\$3-10		4-11	\$4-5\times\$4-10
				2-14	Concat(\$2-7, \$2-11), Conv(128,64,3,1,1)		3-12	Concat(\$3-5, \$3-9), Conv(128,64,3,1,1)		4-12	Concat(\$4-5, \$4-9), Conv(128,64,3,1,1)
				2-15	\$2-7\times\$2-14		3-13	\$3-5\times\$3-12		4-13	\$4-5\times\$4-12
				2-16	Concat(\$2-12, \$2-15, \$2-7), Conv(192,64,3,1,1), LeakyReLU, Conv(64,2,3,1,1), Softmax		3-14	Concat(\$3-11, \$3-13, \$3-5), Conv(192,64,3,1,1), LeakyReLU, Conv(64,2,3,1,1), Softmax		4-14	Concat(\$4-11, \$4-14, \$4-5), Conv(192,64,3,1,1), LeakyReLU, Conv(64,2,3,1,1), Softmax
				2-17	\$2-13\times\$2-16[0]+\$2-15\times\$2-16[1], RB \times 8		3-15	\$3-11\times\$3-14[0]+\$3-13\times\$3-14[1], RB \times 6		4-15	\$4-11\times\$4-14[0]+\$4-13\times\$4-14[1], RB \times 4
				2-18	Conv(64,256,3,1,1), PixelShuffle(2), Conv(64,64)		3-16	Conv(64,256,3,1,1), PixelShuffle(2), Conv(64,64)		4-16	Conv(64,3,3,1,1),

Table 7: Comparison of the model size. *light* denotes the light version of our proposed network. **Red** and **blue** indicate first and second performance, respectively. We include the parameter of discriminator in the total parameters of the GAN-based model.

	Model	Parameters	Tanks and Temple	BlendedMVS	GTAV
SISR	EDSR [21]	43.09M	28.99 / 0.8493 / 0.230	27.80 / 0.7198 / 0.393	30.93 / 0.8478 / 0.211
	RCAN [51]	15.59M	29.89 / 0.8544 / 0.231	27.90 / 0.7227 / 0.393	31.23 / 0.8530 / 0.212
	HAN [27]	16.07M	29.76 / 0.8518 / 0.228	27.86 / 0.7211 / 0.396	31.13 / 0.8515 / 0.206
	ESRGAN [41]	31.20M	26.63 / 0.7720 / 0.112	25.50 / 0.6315 / 0.173	28.26 / 0.7746 / 0.105
	SPSR [25]	39.30M	27.16 / 0.7736 / 0.104	25.72 / 0.6406 / 0.168	28.37 / 0.7739 / 0.102
VSR	RBPNet [10]	12.77M	29.75 / 0.8531 / 0.236	27.79 / 0.7179 / 0.408	31.27 / 0.8559 / 0.218
	RSDN [12]	6.19M	29.00 / 0.8347 / 0.240	26.38 / 0.6412 / 0.480	30.26 / 0.8365 / 0.223
	MuCAN [18]	25.66M	29.90 / 0.8573 / 0.215	27.72 / 0.7162 / 0.400	31.24 / 0.8585 / 0.196
	IconVSR [4]	8.71M	29.75 / 0.8547 / 0.227	27.53 / 0.7089 / 0.408	31.41 / 0.8633 / 0.205
Ref-SR	TTSR [45]	145.66M	27.53 / 0.7858 / 0.124	26.09 / 0.6567 / 0.201	28.80 / 0.7914 / 0.121
	TTSR-rec [45]	6.73M	29.46 / 0.8471 / 0.231	27.68 / 0.7193 / 0.396	30.79 / 0.8485 / 0.216
	MASA [23]	18.99M	26.66 / 0.7545 / 0.134	25.84 / 0.6468 / 0.220	28.05 / 0.7699 / 0.131
	MASA-rec [23]	4.03M	29.67 / 0.8538 / 0.218	27.82 / 0.7335 / 0.375	31.12 / 0.8613 / 0.196
	C^2 -Matching [13]	14.11M	29.29 / 0.8384 / 0.158	27.24 / 0.7039 / 0.281	30.57 / 0.8396 / 0.153
	C^2 -Matching-rec [13]	8.87M	29.89 / 0.8609 / 0.212	27.99 / 0.7377 / 0.370	31.21 / 0.8628 / 0.194
	MVSNet	19.42M	28.83 / 0.8372 / 0.085	26.90 / 0.7080 / 0.182	30.27 / 0.8462 / 0.085
	MVSNet- <i>light</i>	9.67M	28.48 / 0.8260 / 0.090	26.83 / 0.7003 / 0.190	29.89 / 0.8337 / 0.094
	MVSNet-rec	14.18M	30.26 / 0.8748 / 0.191	28.03 / 0.7457 / 0.360	31.60 / 0.8775 / 0.179
	MVSNet- <i>light</i> -rec	4.39M	30.12 / 0.8712 / 0.199	28.00 / 0.7426 / 0.368	31.45 / 0.8735 / 0.186

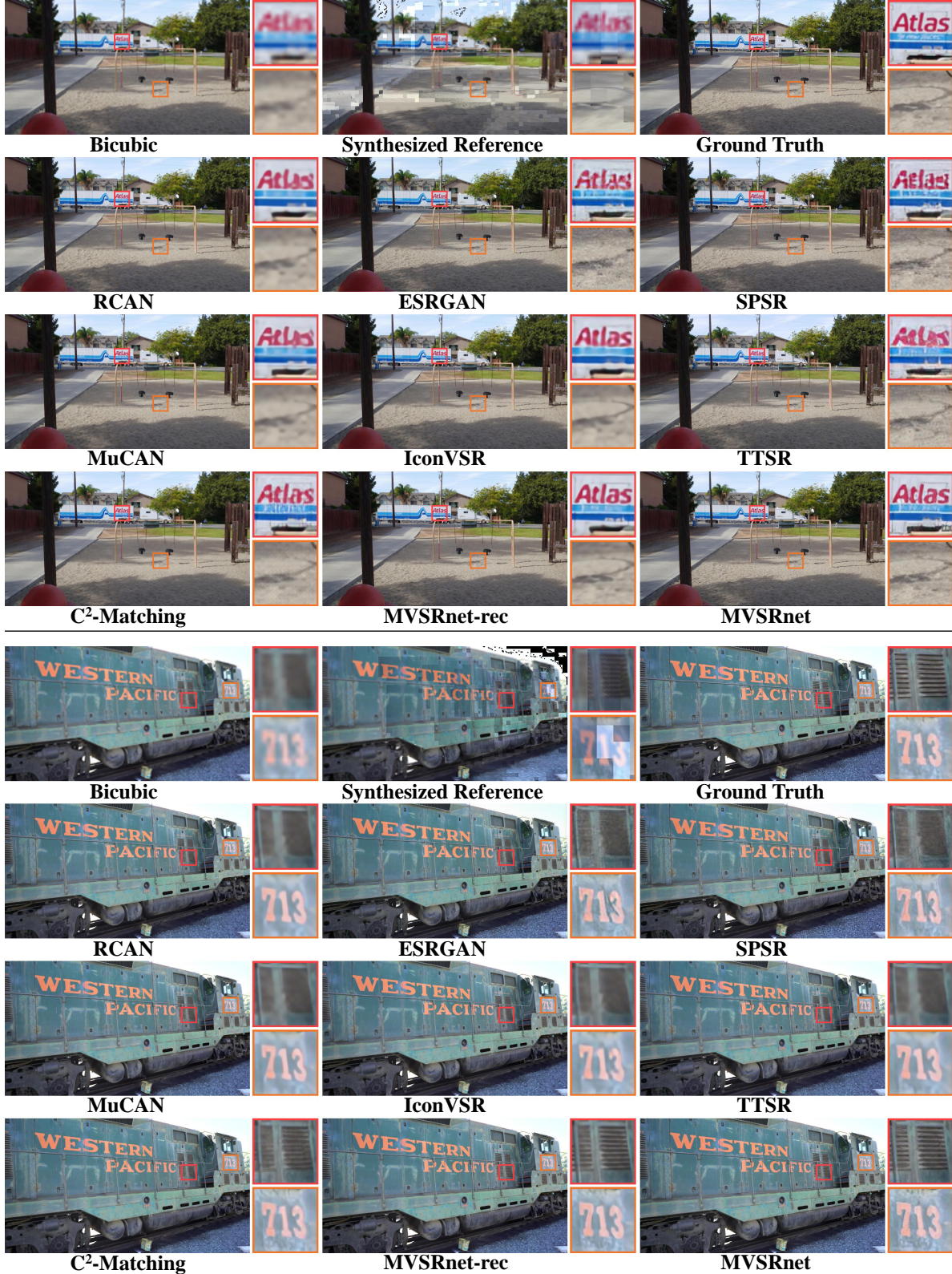


Figure 7: More qualitative comparisons with soft-of-the-art SR methods on the Tanks and Temple [15] dataset.

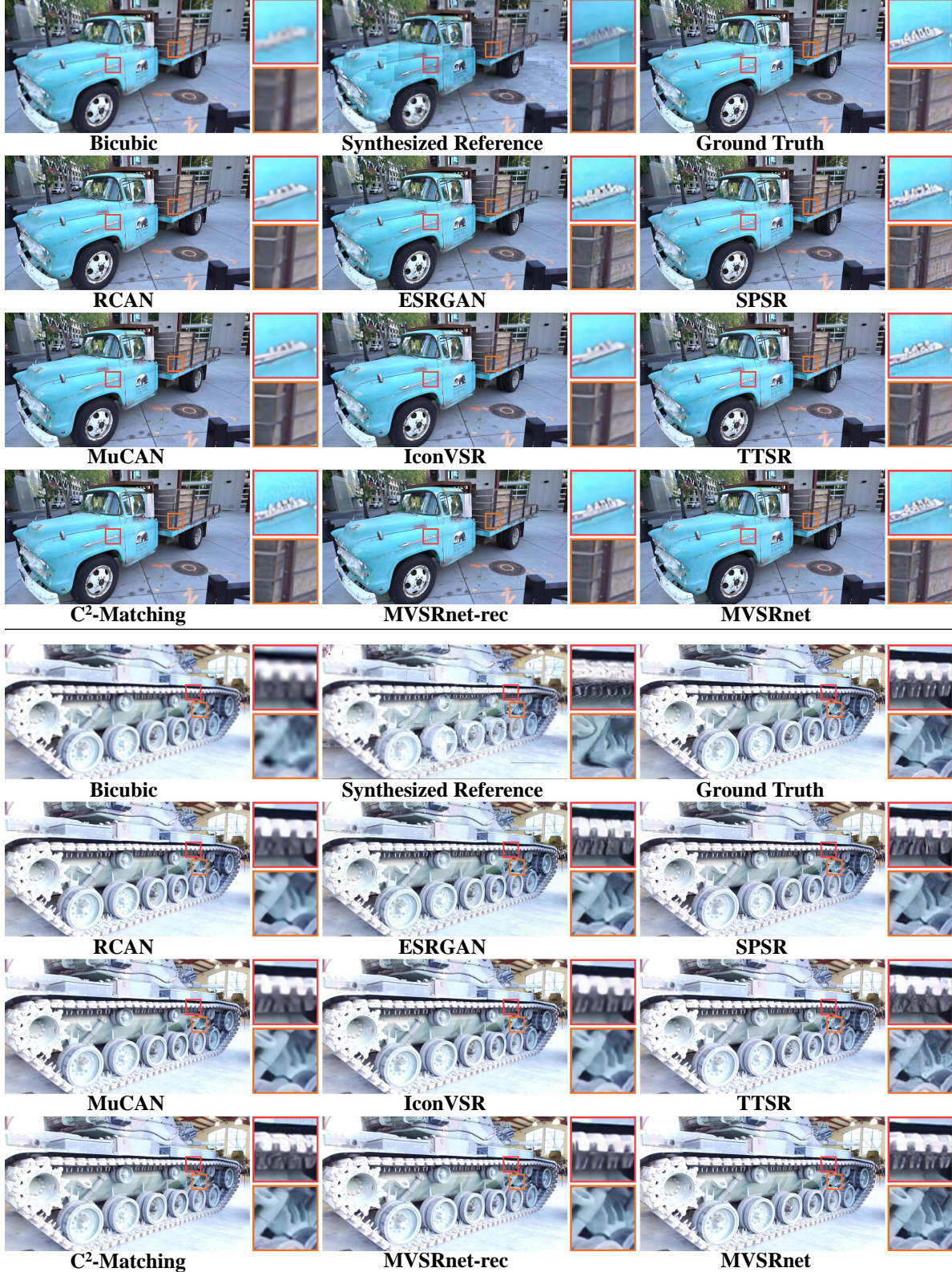


Figure 8: More qualitative comparisons with soft-of-the-art SR methods on the Tanks and Temple [15] dataset.

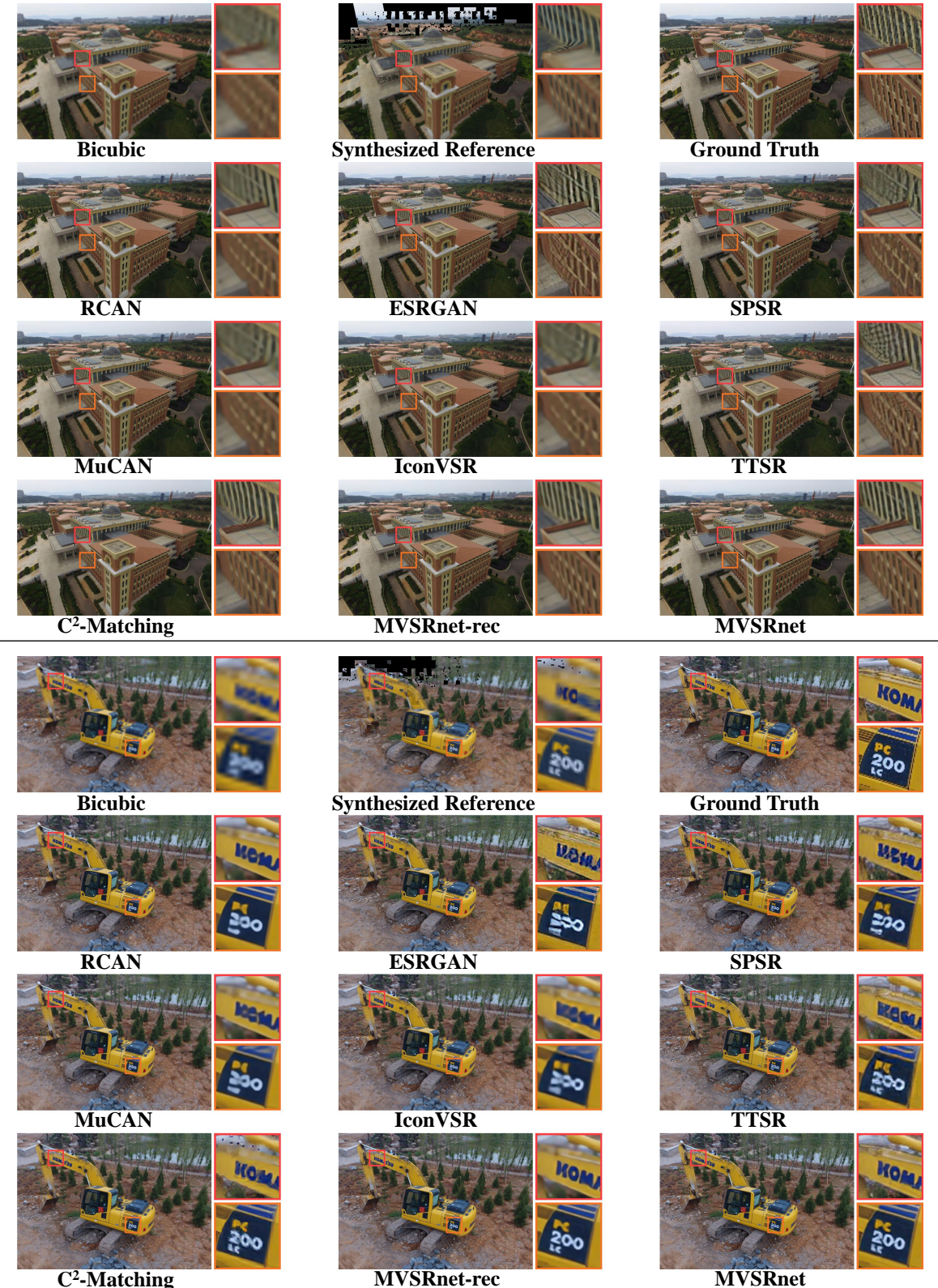


Figure 9: More qualitative comparisons with soft-of-the-art SR methods on the BlendedMVS [47] dataset.



Figure 10: More qualitative comparisons with soft-of-the-art SR methods on the GTAV [11] dataset.